# Multimaterial Topology Design for Optimal Elastic and Thermal Response with Material-Specific Temperature Constraints

Ziliang Kang, Kai A. James

*University of Illinois at Urbana-Champaign, Department of Aerospace Engineering*

*Urbana, Illinois, United States*

**Abstract**

We present an original method for multimaterial topology optimization with elastic and thermal response considerations. The material distribution is represented parametrically using a formulation in which finite element-style shape functions are used to determine the local material properties within each finite element. We optimize a multi-functional structure which is designed for a combination of structural stiffness and thermal insulation. We conduct parallel uncoupled finite element analyses to simulate the elastic and thermal response of the structure by solving the two-dimensional Poisson problem. We explore multiple optimization problem formulations, including structural design for minimum compliance subject to local temperature constraints so that the optimized design serves as both a support structure and a thermal insulator. We also derive and implement an original multimaterial aggregation function that allows the designer to simultaneously enforce separate maximum temperature thresholds based upon the melting point of the various design materials. The nonlinear programming problem is solved using gradient-based optimization with adjoint sensitivity analysis. We present results for a series of two-dimensional example problems. The results demonstrate that the proposed algorithm consistently converges to feasible multimaterial designs with the desired elastic and thermal performance.

*Keywords:* Elasticity, Finite element methods, Structures, Thermal effects, Topology design

## 1. Introduction

Topology optimization was first introduced by Bendsøe and Kikuchi in 1988 [1], as a homogenization-based method for obtaining optimal material layouts. Unlike size and shape optimization, topology optimization modifies the full material layout and topology throughout the design domain. Therefore, it is able to generate drastic changes in the mechanical performance and functionality of the structure. With the development of additive manufacturing, structures designed by topology optimization are easier to fabricate than ever before [2], which has inspired a renewed focus on topology optimization for designing multi-functional and multimaterial structures. Despite the relative maturity of the field, few authors have explored the design of multimaterial, multi-functional structures that combine optimal elastic and thermal performance. Previous studies have individually addressed the topics of elastic response, thermal response and multimaterial design, and have successfully solved various benchmark problems [3, 4, 5].

Topology optimization of elastic problems remains a widely studied research area that includes studies on stress constraints [6, 7, 8], extreme thermal expansion [9, 10, 11], and elastoplastic structures [12, 13, 14]. In terms of topology optimization for the steady-state heat conduction problem, Bendsøe and Sigmund first proposed that such structures should be branch-like and have

venation for an efficient transmission of heat energy [5]. Other researches in this area focused on efficiently obtaining results for the thermal conductivity problem. Li et al. implemented an evolutionary method in 2004 [15], and Zhuang et al. used a level-set method in 2007 [16]. More recently, Lohan et al. compared results generated by the SIMP method with results from a space colonization algorithm [17] to study 2D topology optimization involving heat conduction. While most authors have relied on finite element analysis to simulate the thermal response, Gersborg-Hansen et al. used the finite volume method to solve the 2D topology optimization problem and also obtained a tree-like result [18]. Efforts in the area have also been directed to extending the problem to a three-dimensional domain. Dede [19], Chen et al. [20] and Burger [21] successfully confirmed that the optimized structure for heat conduction should remain branch-like in the 3D problem. Researchers have also considered heat convection problems together with the topology optimization problem of heat conduction for various special cases [22, 23, 24]. One study from de Kruijf et al. in 2007 combines thermal conductivity and elasticity, by setting multiple objectives for a single-material optimization problem [25]. Their results show that such problems will result in a structure with the combined features of trusses and venation. However, multimaterial cases and more practical applications still remain unexplored.

It is our hypothesis that allowing for multiple materials provides the optimizer with greater freedom to pursue multiple competing objectives as compared with single-material optimization. Bendsøe and Simgund first proposed a SIMP material interpolation formulation for two materials plus void elements in 1988 [26], which remains a popular method for multimaterial topology optimization [27, 28, 29]. Later, Gao et al. proposed a modified formulation for three materials plus void elements [30]. Another widely adopted method for multimaterial representation is the multi-material level set method in which a unique level-set function is optimized for each material phase [31, 32, 33].

Similar versions of the multiphase design problem have arisen in other application domains, such as the design of composite layups, where the ply angles of the composite layers must conform to a discrete set of admissible angles due to manufacturing considerations. In this context, the play angles are analogous to the material phases found in the multimaterial topology optimization problem. For the composite layup design task, Bruyneel et al. [36] introduced a parameterization scheme in which the local ply angle was represented by a set of shape functions similar to those found in the isoparametric finite element formulation. The shape functions were penalized in order to encourage convergence to discrete values, and eliminate intermediate ply angles from the optimized design. Consequently, they coined the method, *shape functions with penalization* (SFP). In 2017, James applied the SFP method to the multimaterial topology optimization problem, and introduced a novel modification to enable simultaneous topology design with optimal material selection [34].

This study endeavors to extend that framework by applying it to multimaterial topology optimization problems containing both elastic and thermal considerations. In this paper, we choose the general case of a 2D structure with linear elastic properties and steady-state temperature distribution. Since both the elastic response and the thermal response of the domain are linear and uncoupled, we separately implement two finite element analyses to model both responses, and use a SFP formulation to allow for three design materials plus void. In this paper, several key contributions are made, beginning with the extension of the SFP formulation to the multiphysics problem containing elastic and thermal response. Additionally, we introduce novel constraint formulations for enforcing regional maximum temperature constraints and material-specific local temperature constraints within the multimaterial structure.

## 2. Methodology

Using a multimaterial framework, the design task is treated as a material distribution problem in accordance with the topology optimization method. We use uncoupled linear finite element analyses to model the linear elastic response and steady-state temperature distribution in the structural domain. To quantify the impact of expanding the design space to include multiple materials, we solve both the single-material problem and multimaterial problem, and compare the performance of the optimized designs obtained by each approach. In addition, we also study the results produced by different combinations of objective and constraint functions.

### *2.1. The Combined Thermoelastic Design Problem*

For the initial benchmark problem, the design domain is selected to be a 12m×2m MBB beam domain with load $p = 100$kN at the top center and fixed temperature $\overline{T} = 100°$C at the bottom center. The depth of the beam (in the $z$-direction) is 1m. A fixed heat flux $q = 50\text{w/m}^2$ is applied to the outer surface of the beam. There is no distributed heat source within the volume of the structure.

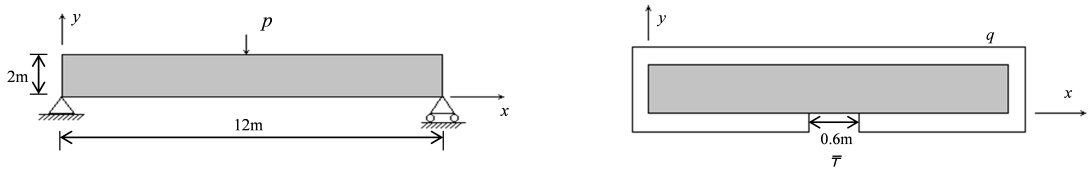


(a) The elasticity problem

(b) The thermal conductivity problem

Figure 1: Geometry and boundary conditions for the combined thermoelastic design problem

We set the multimaterial beam to be composed of three materials plus void elements. The three materials are distinctly different in their properties, in order to allow the user to exploit these differences to pursue the various design objectives and constraints. The three materials are Sn96.5/Ag3.0/Cu0.5 (SAC305), Beryllium Copper (BC) and Aluminum-Silicon-Carbide Composite (Al-SiC). Their mechanical and thermal properties [35] are shown below in Table 1.

| Material | Void | SAC305 | BC | Al-SiC |
|---|---|---|---|---|
| $E$(GPa) | $10^{-9}$ | 51 | 131 | 188 |
| $\kappa$(W/(m·°C)) | 0.5 | 59 | 105 | 200 |
| Melting Point(°C) | - | 217-218 | 865 - 955 | 557 - 613 |

Table 1: Material properties

### *2.2. Finite Element Analysis*

We use square finite elements to analyze the elastic and thermal responses of the design domain. The elastic and thermal governing equations for the design domain are shown in equation 1 and

equation 5. For the elastic problem, we apply the plane stress formula. Its governing differential equation is given by

$$\begin{aligned} &\text{Elastic GDE}: \quad \begin{bmatrix} \frac{\partial}{\partial x} & 0 & \frac{\partial}{\partial y} \\ 0 & \frac{\partial}{\partial y} & \frac{\partial}{\partial x} \end{bmatrix} \begin{bmatrix} \sigma_{xx} \\ \sigma_{yy} \\ \sigma_{xy} \end{bmatrix} + \begin{bmatrix} b_x \\ b_y \end{bmatrix} = \boldsymbol{D}^T \boldsymbol{\sigma}_v + \boldsymbol{b} = \begin{bmatrix} 0 \\ 0 \end{bmatrix} \\ &\text{Boundary Equation}: \boldsymbol{\sigma n} + \boldsymbol{f} = 0 \end{aligned} \tag{1}$$

where $\boldsymbol{b}$ is the body force vector which equals 0 for this problem, $\boldsymbol{\sigma}_v$ is the two-dimensional Cauchy stress tensor expressed in Voigt notation, $\boldsymbol{f}$ is the traction force vector and $\boldsymbol{n}$ is the unit normal on the surface to which the traction is applied. The relationship between strain, $\boldsymbol{\varepsilon}$, and displacement, $\boldsymbol{u}$, is defined by the matrix $\boldsymbol{D}$

$$\begin{aligned} \boldsymbol{\varepsilon}_v &= \boldsymbol{D}\boldsymbol{u} \\ \boldsymbol{D} &= \begin{bmatrix} \frac{\partial}{\partial x} & 0 \\ 0 & \frac{\partial}{\partial y} \\ \frac{\partial}{\partial y} & \frac{\partial}{\partial x} \end{bmatrix} \end{aligned} \tag{2}$$

Finally, the relationship between stress $\boldsymbol{\sigma}$ and strain $\boldsymbol{\varepsilon}$ is defined by the constitutive matrix $\boldsymbol{E}$ for the two-dimensional plain stress problem, as shown below.

$$\begin{aligned} \boldsymbol{\sigma}_v &= \boldsymbol{E}\boldsymbol{\varepsilon}_v \\ \boldsymbol{E} &= \frac{E}{1-\nu^2} \begin{bmatrix} 1-\nu & \nu & 0 \\ \nu & 1-\nu & 0 \\ 0 & 0 & \frac{1}{2}(1-2\nu) \end{bmatrix} \end{aligned} \tag{3}$$

where $E$ is Young's modulus and $\nu$ is the Poisson's ratio which we have set to be 0.3 in the examples that follow. The applied force in the elasticity problem has a magnitude of $p = 100$kN. The boundary value problem described above is discretized using a uniform grid of square isoparametric finite elements so that the resulting equilibrium equation can be written as follows.

$$\begin{bmatrix} \boldsymbol{K}^e_{ff} & \boldsymbol{K}^e_{fc} \\ \boldsymbol{K}^e_{cf} & \boldsymbol{K}^e_{cc} \end{bmatrix} \begin{bmatrix} \boldsymbol{u}_f \\ \boldsymbol{u}_c \end{bmatrix} - \begin{bmatrix} \boldsymbol{F}_f \\ \boldsymbol{F}_c \end{bmatrix} = 0 \tag{4}$$

where $\boldsymbol{K}^e$ is the stiffness matrix of the elastic problem, $\boldsymbol{u}$ is the global vector of nodal displacements, and $\boldsymbol{F}$ is the global consistent force vector. Here we have partitioned the linear system into blocks corresponding to the free ($f$) and constrained ($c$) degrees of freedom, which we will later use when deriving the adjoint sensitivity analysis formulas.

The thermal response of the structure is governed by the boundary value problem given in Eqn. 5. Here, $\kappa$ is the thermal conductivity of the design material, $Q$ is the internal heating source which equals 0 in the example presented, $T$ is the temperature field, and $q$ heat flux at the surface. Note that $\boldsymbol{n}_x$ and $\boldsymbol{n}_y$ are $x$ and $y$ components of the unit outward normal vector.

$$\begin{aligned} &\text{Thermal GDE}: \quad \kappa_x \frac{\partial^2 T}{\partial x^2} + \kappa_y \frac{\partial^2 T}{\partial y^2} + Q = 0 \\ &\text{Boundary Condition}: \overline{T} = 100^{\circ}\text{C along } \partial\Omega_T; \\ &\kappa_x \frac{\partial T}{\partial x}\boldsymbol{n}_x + \kappa_y \frac{\partial T}{\partial y}\boldsymbol{n}_y + q = 0, \ q = 50w/m^2 \text{ along } \partial\Omega_q = \partial\Omega/\partial\Omega_T. \end{aligned} \tag{5}$$

Similar to the elasticity problem, the finite element discretization of the thermal problem leads to a linear algebraic system as shown in equation 6

$$\begin{bmatrix} \boldsymbol{K}^t_{ff} & \boldsymbol{K}^t_{fc} \\ \boldsymbol{K}^t_{cf} & \boldsymbol{K}^t_{cc} \end{bmatrix} \begin{bmatrix} \boldsymbol{T}_f \\ \boldsymbol{T}_c \end{bmatrix} - \begin{bmatrix} \boldsymbol{q}_f \\ \boldsymbol{q}_c \end{bmatrix} = 0 \tag{6}$$

Hese $\boldsymbol{K}^t$ is the thermal stiffness matrix, $\boldsymbol{T}$ is vector of nodal temperatures, and $\boldsymbol{q}$ is the heat flux vector, all of which have been partitioned into blocks corresponding to the free and constrained degrees of freedom.

*2.3. Design Parameterization*

We treat the design task as a material distribution problem in which we optimally distributed multiple design materials throughout the working domain the pursue a given objective. In the current study, the design materials are characterized by their Young's modulus (i.e. elastic stiffness), and their thermal conductivity. The material distribution is represented parametrically using the *Shape Functions with Penalization* (SFP) method. This approach was first used in composite design by Bruyneel et al. [36] and Gao et al.[37] and then was adapted to the topology optimization problem by James [34]. Under this formulation, the Young's modulus, $E_i$, and thermal conductivity, $\kappa_i$, of each element, $i$, is evaluated as a weighted sum of the the respective properties of all available material phases, and can be expressed as

$$\begin{aligned} E_i &= \sum_{j=1}^{m} \mu_i^{(j)} E^{(j)} \\ \kappa_i &= \sum_{j=1}^{m} \mu_i^{(j)} \kappa^{(j)} \end{aligned} \tag{7}$$

where the weights, $\mu^{(j)}$, are a set of *activation* functions and have the form shown in equation 8

$$\begin{aligned} \mu^{(1)} &= r_1^P r_2^P \\ \mu^{(2)} &= r_1^P (1 - r_2)^P \\ \mu^{(3)} &= (1 - r_1)^P r_2^P \\ \mu^{(4)} &= (1 - r_2)^P (1 - r_1)^P \end{aligned} \tag{8}$$

In equation 8, $r_1, r_2 \in [0, 1]$ are independent variables, directly selected by the optimizer, and $P$ is a penalization factor. Both the Young's modulus and thermal conductivity are penalized to guarantee that there is only one material in each element, and that the volume ratio of each element is the same for both design parameters [25]. Once the local effective Young's modulus and thermal conductivity of each element are computed, this information is assembled to construct the global elastic and thermal stiffness matrices used in the finite element analysis equations (equations 4 and 6 respectively), to solve the global displacement and temperature distributions.

*2.4. Functions of Interest*

*2.4.1. The Combined Elastic and Thermal Objective Function*

In the first set of example problems, the objective function is a summation of the normalized elastic compliance (i.e. strain energy) and the normalized average temperature of the design domain excluding void area. The resulting function has the following form,

$$f_{obj} = \frac{\boldsymbol{F}^T \boldsymbol{u}}{\boldsymbol{F}^T \boldsymbol{u}_0} + \left( \frac{\sum_{i=1}^{n} (1 - \mu_i^{(1)}) T_i}{\sum_{i=1}^{n} (1 - \mu_i^{(1)})} \right) / \left( \frac{\sum_{i=1}^{n} (1 - \mu_{0_i}^{(1)}) T_{0_i}}{\sum_{i=1}^{n} (1 - \mu_{0_i}^{(1)})} \right) \tag{9}$$

where $\boldsymbol{F}$ global vector of nodal forces used in the finite element analysis, and $T_i$ is the approximate average temperature in element $i$, based on a one-point Gauss quadrature integration, as defined in equation 10, where $T_i^{(ei)}$ is the temperature value at node $ei$ within element $i$. Note also that $\mu^{(1)}$ is the activation function of the void phase, therefore by pre-multiplying each element's average temperature by $(1-\mu_i^{(1)})$, we effectively filter out all void elements from the summation.

$$T_i = \sum_{ei=1}^{4} \frac{1}{4} T_i^{(ei)} \tag{10}$$

For both the elastic and thermal terms, the compliance and average temperature are normalized with respect to their initial values corresponding to the baseline structure, which serves as the starting point for the optimization search. In equation 9, the subscript, 0, indicates the baseline value for a given parameter.

*2.4.2. Temperature-Based Constraints*

In the case of a thermal insulator, we may wish to limit the maximum temperature on an exposed surface. For the design domain shown in Figure 1 we directly enforce a constraint on the temperature along the top surface of the structure, where elements on the top surface are numbered from $n$ to $m$. We sum over each element within this range, and take the $p$-norm aggregate of the normalized average temperature of within each element ($T_i$). Again, we use the coefficient $(1-\mu_i^{(1)})$ so that any void elements within the prescribed range are omitted from the summation. The $p$-norm function allows us to obtain a smooth approximation of the maximum local temperature. The resulting formulation of the constraint function is given by

$$g = \left[ \sum_{i=n}^{m} \left( (1-\mu_i^{(1)})^{\eta} \frac{T_i}{T^*} \right)^p \right]^{1/p} \leq 1 \tag{11}$$

where $T^*$ is the maximum allowable temperature. For large values of the aggregation parameter $p$, the function approaches the maximum normalized temperature along the chosen surface. The parameter $\eta$ is an additional constant used to promote stable convergence of the optimization search. In the examples presented, we select $p$ and $\eta$ to have values of 10 and 0.8 respectively.

In other design problems, we wish to set a unique temperature constraint for each material used in the design. This type of constraint may be useful if the primary concern is preventing melting or viscoelastic creep within the material. In this case, the maximum allowable temperature is specific to the material, therefore we must set separate temperature limits $T^{*(j)}$ for each design material. The SFP formulation used in this study provides an effective and numerically efficient means of enforcing a single global temperature constraint that is specific to each material within the structure. This constraint function is shown in equation 12.

$$g = \left[ \sum_{i=1}^{N} \left( \sum_{j=2}^{4} (\mu_i^{(j)})^{\eta} \frac{T_i}{T^{*(j)}} \right)^p \right]^{1/p} \leq 1 \tag{12}$$

Note that we sum over all elements in the domain, and for each element we take a weighted sum of the quantity given by $(\mu_i^{(j)})^{\eta} \frac{T_i}{T^{*(j)}}$. If element $i$ contains the non-void material phase $j$, then the sum $\sum_{j=2}^{4} (\mu_i^{(j)})^{\eta} \frac{T_i}{T^{*(j)}}$ will contain only one non-zero term, which reduces to $\frac{T_i}{T^{*(j)}}$, such that the average temperature of element $i$ is normalized with respect to the maximum temperature threshold corresponding to the specific material contained within that element. For any converged

design in which all elements contain only one material, this constraint will be satisfied only if, for any element $i$ containing material $j$, the average temperature within that element $T_i$, is equal to or less than the maximum allowable temperature, $T^{*(j)}$, for material $j$.

*2.5. Sensitivity Analysis*

Due to the high dimensionality of the design space associated with the multimaterial topology optimization problem, we use gradient-based methods to solve the numerical optimization problem. In this paper, we choose Method of Moving Asymptotes (MMA) [41] to solve the nonlinear programming problem. To compute the design sensitivities, we use the adjoint method, which begins by rewriting the finite element equilibrium equation (4) in residual form $\boldsymbol{R}^e = \boldsymbol{0}$, as shown in equation 13. The thermal problem (equation 6) also has an analogous residual form $\boldsymbol{R}^t = \boldsymbol{0}$.

$$\begin{bmatrix} \boldsymbol{R}_f^e \\ \boldsymbol{R}_c^e \end{bmatrix} = \begin{bmatrix} \boldsymbol{K}_{ff}^e & \boldsymbol{K}_{fc}^e \\ \boldsymbol{K}_{cf}^e & \boldsymbol{K}_{cc}^e \end{bmatrix} \begin{bmatrix} \boldsymbol{u}_f \\ \boldsymbol{u}_c \end{bmatrix} - \begin{bmatrix} \boldsymbol{F}_f \\ \boldsymbol{F}_c \end{bmatrix} = 0 \tag{13}$$

The sensitivity analysis of the elastic problem is well-known and can be found in reference [5]. Hence we devote this section to discussing the sensitivity analysis of the thermal problem.

*2.5.1. Differentiating the Average Temperature Function*

For the objective combining both elastic compliance and the average temperature, as shown in equation 9, we can separately discuss the sensitivities of the elastic term and the thermal term since they are uncoupled from each other. Hence, here we extract the thermal portion of the function (equation 9) and discuss its sensitivity. We define the new objective as

$$f_{obj} = \frac{\sum_{i=1}^{n}(1-\mu_i^{(1)})T_i}{\sum_{i=1}^{n}(1-\mu_i^{(1)})}. \tag{14}$$

Then we form the augmented Lagrangian function by adding the residual term $\boldsymbol{R}^t$.

$$\Pi(\boldsymbol{T}_f, \boldsymbol{r}) = f(\boldsymbol{T}_f, \boldsymbol{r}) + \boldsymbol{\lambda}_f^T \boldsymbol{R}_f^t(\boldsymbol{T}_f, \boldsymbol{r}) + \boldsymbol{\lambda}_c^T \boldsymbol{R}_c^t(\boldsymbol{T}_f, \boldsymbol{r}) \tag{15}$$

Note that the vector $\lambda^T = [\lambda_f^T, \lambda_c^T]$ is a free parameter, whose value we will subsequently select to minimize computational effort. Differentiating the augmented expression 15 with respect to $\boldsymbol{r}$, we have

$$\frac{\mathrm{d}\Pi}{\mathrm{d}\boldsymbol{r}} = \frac{\partial f}{\partial \boldsymbol{r}} + \boldsymbol{\lambda}_f^T \frac{\partial \boldsymbol{R}_f^t}{\partial \boldsymbol{r}} + \boldsymbol{\lambda}_c^T \frac{\partial \boldsymbol{R}_c^t}{\partial \boldsymbol{r}} + \left[ \frac{\partial f}{\partial \boldsymbol{T}_f} + \boldsymbol{\lambda}_f^T \frac{\partial \boldsymbol{R}_f^t}{\partial \boldsymbol{T}_f} + \boldsymbol{\lambda}_c^T \frac{\partial \boldsymbol{R}_c^t}{\partial \boldsymbol{T}_f} \right] \frac{\mathrm{d}\boldsymbol{T}_f}{\mathrm{d}\boldsymbol{r}}, \tag{16}$$

where the operator $\partial/\partial \boldsymbol{r}$ denotes *explicit* derivatives, which capture only direct dependence. By contrast, *implicit* derivatives, denoted $\mathrm{d}/\mathrm{d}\boldsymbol{r}$, capture any indirect dependence the function may have with respect to $\boldsymbol{r}$, due to the solution of the residual equation. Consequently, implicit derivatives are much more costly to evaluate, and this operation should be avoided if possible.

To eliminate the implicit terms in equation 16, we select the adjoint solution for the parameters $\boldsymbol{\lambda}_f$ and $\boldsymbol{\lambda}_c$, which yields

$$\begin{cases} \boldsymbol{\lambda}_c = 0 \\ \boldsymbol{\lambda}_f = -{\boldsymbol{K}_{ff}^t}^{-1} \frac{\partial f_{obj}}{\partial \boldsymbol{T}_f} \end{cases} \tag{17}$$

Then the differentiation of the augmented Lagrangian expression (equation 15) becomes

$$\frac{\mathrm{d}f_{obj}}{\mathrm{d}\boldsymbol{r}} = \frac{\partial f_{obj}}{\partial \boldsymbol{r}} - \begin{bmatrix} {\boldsymbol{K}_{ff}^t}^{-1} \frac{\partial f_{obj}}{\partial \boldsymbol{T}_f} \\ 0 \end{bmatrix}^T \frac{\partial \boldsymbol{K}^t}{\partial \boldsymbol{r}} \boldsymbol{T} \tag{18}$$

Substituting equation 7 into the equation above, we can ultimately get the following derivative formula with respect to the local design parameter vector $\boldsymbol{r}_i = [r_{i1}, r_{i2}]^T$

$$\frac{\mathrm{d}f_{obj}}{\mathrm{d}\boldsymbol{r}_i} = \frac{\partial f_{obj}}{\partial \boldsymbol{r}_i} - \frac{\partial \mu_i^{(j)}}{\partial \boldsymbol{r}_i}\kappa^{(j)}\left[\tilde{\boldsymbol{t}}_{ei}^T \overline{\boldsymbol{k}^t}_{ei}\boldsymbol{t}_{ei}\right] \tag{19}$$

where $\boldsymbol{t}_{ei}$ is the nodal temperature vector of element $i$, and $\overline{\boldsymbol{k}^t}_{ei}$ is the normalized element thermal stiffness matrix of element $i$, which is a function to the local element thermal conductivity $\kappa_i$, so that $\overline{\boldsymbol{k}^t}_{ei} = \boldsymbol{k}^t{}_{ei}/\kappa_i$. Here, $\tilde{\boldsymbol{t}}_{ei}$ is the local quasi-temperature vector of element $i$, which is extracted from the global quasi-temperature vector $\widetilde{\boldsymbol{T}}$ given by

$$\widetilde{\boldsymbol{T}} = \begin{bmatrix} \boldsymbol{K}_{ff}^t{}^{-1}\frac{\partial f_{obj}}{\partial \boldsymbol{T}_f} & 0 \end{bmatrix}^T \tag{20}$$

Taking the partial derivative of $f_{obj}$ with respect to $\boldsymbol{r}_i$, we have

$$\frac{\partial f_{obj}}{\partial \boldsymbol{r}_i} = \frac{\sum_{j=1}^n (1-\mu_j^{(1)})T_j - \sum_{j=1}^n (1-\mu_j^{(1)})T_j}{\left(\sum_{j=1}^n (1-\mu_j^{(1)})\right)^2} \cdot \frac{\partial (1-\mu_i^{(1)})}{\partial \boldsymbol{r}_i} = 0 \tag{21}$$

For the partial derivative of $f_{obj}$ with respect to $\boldsymbol{T}_f$, knowing that $\boldsymbol{T}_f = [t_f^{(1)} \cdots t_f^{(s)}]^T$ has length $s$, we have

$$\frac{\partial f_{obj}}{\partial \boldsymbol{T}_f} = \frac{1}{\sum_{i=1}^n (1-\mu_i^{(1)})} \cdot \begin{bmatrix} \sum_{i=1}^n (1-\mu_i^{(1)})\varphi_i^{(1)} \\ \vdots \\ \sum_{i=1}^n (1-\mu_i^{(1)})\varphi_i^{(s)} \end{bmatrix}_{s\times 1}, \tag{22}$$

where

$$\varphi_i^{(l)} = \frac{\partial T_i}{\partial t_f^{(l)}} = \begin{cases} 1/4 & \text{if } \frac{\partial T_i}{\partial t_f^{(l)}} \neq 0 \\ 0 & \text{if } \frac{\partial T_i}{\partial t_f^{(l)}} = 0 \end{cases}, l = 1, \cdots, s. \tag{23}$$

*2.5.2. Differentiating the Maximum Local Temperature Function*

For the maximum local temperature function, shown in equation 11, we can express the augmented Lagrangian expression as

$$\Pi(\boldsymbol{T}_f, \boldsymbol{q}_c, \boldsymbol{r}) = g(\boldsymbol{T}_f, \boldsymbol{q}_c, \boldsymbol{r}) + \boldsymbol{\lambda}_f^T \boldsymbol{R}_f^t(\boldsymbol{T}_f, \boldsymbol{q}_c, \boldsymbol{r}) + \boldsymbol{\lambda}_c^T \boldsymbol{R}_c^t(\boldsymbol{T}_f, \boldsymbol{q}_c, \boldsymbol{r}) \tag{24}$$

Differentiating the above equation with respect to $\boldsymbol{r}$, we have

$$\begin{aligned} \frac{\mathrm{d}\Pi}{\mathrm{d}\boldsymbol{r}} =& \frac{\partial g}{\partial \boldsymbol{r}} + \boldsymbol{\lambda}_f^T \frac{\partial \boldsymbol{R}_f^t}{\partial \boldsymbol{r}} + \boldsymbol{\lambda}_c^T \frac{\partial \boldsymbol{R}_c^t}{\partial \boldsymbol{r}} + \left[\frac{\partial g}{\partial \boldsymbol{T}_f} + \boldsymbol{\lambda}_f^T \frac{\partial \boldsymbol{R}_f^t}{\partial \boldsymbol{T}_f} + \boldsymbol{\lambda}_c^T \frac{\partial \boldsymbol{R}_c^t}{\partial \boldsymbol{T}_f}\right] \frac{\mathrm{d}\boldsymbol{T}_f}{\mathrm{d}\boldsymbol{r}} \\ &+ \left[\frac{\partial g}{\partial \boldsymbol{q}_c} + \boldsymbol{\lambda}_f^T \frac{\partial \boldsymbol{R}_f^t}{\partial \boldsymbol{q}_c} + \boldsymbol{\lambda}_c^T \frac{\partial \boldsymbol{R}_c^t}{\partial \boldsymbol{q}_c}\right] \frac{\mathrm{d}\boldsymbol{q}_c}{\mathrm{d}\boldsymbol{r}} \end{aligned} \tag{25}$$

To eliminate the implicit terms in equation 25, we obtain the adjoint solution for the parameters $\boldsymbol{\lambda}_f$ and $\boldsymbol{\lambda}_c$, which is given by

$$\begin{cases} \boldsymbol{\lambda}_c = -\frac{\partial g}{\partial \boldsymbol{q}_c} = 0 \\ \boldsymbol{\lambda}_f = \boldsymbol{K}_{ff}^t{}^{-1}\left[\boldsymbol{K}_{cf}^t \frac{\partial g}{\partial \boldsymbol{q}_c} - \frac{\partial g}{\partial \boldsymbol{T}_f}\right] = -\boldsymbol{K}_{ff}^t{}^{-1}\frac{\partial g}{\partial \boldsymbol{T}_f} \end{cases} \tag{26}$$

The differentiation of the augmented equation 24 then becomes

$$\frac{\mathrm{d}g}{\mathrm{d}\boldsymbol{r}_i} = \frac{\partial g}{\partial \boldsymbol{r}_i} - \begin{bmatrix} {\boldsymbol{K}^t_{ff}}^{-1} \frac{\partial g}{\partial \boldsymbol{T}_f} \\ 0 \end{bmatrix}^T \frac{\partial \boldsymbol{K}^t}{\partial \boldsymbol{r}_i} \boldsymbol{T} \tag{27}$$

Similar to the previous case of equation 19, by substituting equation 7 into the equation above, we can ultimately obtain the final form of the derivative of the augmented equation as

$$\frac{\mathrm{d}g}{\mathrm{d}\boldsymbol{r}_i} = \frac{\partial g}{\partial \boldsymbol{r}_i} - \frac{\partial \mu_i^{(j)}}{\partial \boldsymbol{r}_i} \kappa^{(j)} \left[ \tilde{\boldsymbol{t}}_{ei}^T \overline{\boldsymbol{k}^t}_{ei} \boldsymbol{t}_{ei} \right], \tag{28}$$

where the definition of local quasi-temperature vector $\tilde{\boldsymbol{t}}_{ei}$, local temperature vector $\boldsymbol{t}_{ei}$ and local stiffness matrix $\overline{\boldsymbol{k}^t}_{ei}$ are as defined previously in equation 19. In the sensitivity calculation for these temperature-based constraint functions, we define global the quasi-temperature vector $\widetilde{\boldsymbol{T}}$ assembled from the local quasi-temperature vector $\tilde{\boldsymbol{t}}_{ei}$ as shown in equation 29 below.

$$\widetilde{\boldsymbol{T}} = \begin{bmatrix} {\boldsymbol{K}^t_{ff}}^{-1} \frac{\partial g}{\partial \boldsymbol{T}_f} & 0 \end{bmatrix}^T \tag{29}$$

In the case of a single temperature limit $T^*$ for all design materials, where $g$ is as defined in equation 11, the derivative $\partial g / \partial r_i^{(j)}$ is given by

$$\frac{\partial g}{\partial \boldsymbol{r}_i} = \begin{cases} \left[ \sum_{j=n}^{m} \left( (1-\mu_j^{(1)})^\eta \frac{T_i}{T^*} \right)^p \right]^{\frac{1}{p}-1} \cdot \eta (1-\mu_i^{(1)})^{\eta p - 1} \left( \frac{T_i}{T^*} \right)^p \frac{\partial (1-\mu_i^{(1)})}{\partial \boldsymbol{r}_i} & \text{if } i \in [n,m] \\ 0 & \text{if } i \notin [n,m] \end{cases} \tag{30}$$

Substituting the average temperature $T_i$ in each element $i$ (as defined in equation 10) and knowing that $\boldsymbol{T}_f = [t_f^{(1)} \cdots t_f^{(s)}]^T$ has length $s$, we obtain the partial derivative of $g$ with respect to $\boldsymbol{T}_f$ as

$$\frac{\partial g}{\partial \boldsymbol{T}_f} = \left[ \sum_{i=n}^{m} \left( (1-\mu_i^{(1)})^\eta \frac{T_i}{T^*} \right)^p \right]^{\frac{1}{p}-1} \cdot \begin{bmatrix} \sum_{i=n}^{m} \left( \frac{(1-\mu_i^{(1)})^\eta}{T^*} \right)^p T_i^{p-1} \varphi_i^{(1)} \\ \vdots \\ \sum_{i=n}^{m} \left( \frac{(1-\mu_i^{(1)})^\eta}{T^*} \right)^p T_i^{p-1} \varphi_i^{(s)} \end{bmatrix}_{s \times 1} \tag{31}$$

where

$$\varphi_i^{(l)} = \frac{\partial T_i}{\partial t_f^{(l)}} = \begin{cases} 1/4 & \text{if } \frac{\partial T_i}{\partial t_f^{(l)}} \neq 0 \\ 0 & \text{if } \frac{\partial T_i}{\partial t_f^{(l)}} = 0 \end{cases}, \; l = 1, \cdots, s. \tag{32}$$

For the case where we require a unique temperature limit $T^{*(j)}$ for each design material, where $g$ is defined in equation 12, the derivative $\partial g / \partial r_i^{(j)}$ is given by

$$\frac{\partial g}{\partial \boldsymbol{r}_i} = \begin{cases} \left[ \sum_{k=n}^{m} \left( \sum_{j=2}^{4} (\mu_k^{(j)})^\eta \frac{T_k}{T^{*(j)}} \right)^p \right]^{\frac{1}{p}-1} \cdot \left[ \sum_{j=2}^{4} \eta (\mu_i^{(j)})^{\eta p - 1} \left( \frac{T_i}{T^{*(j)}} \right)^p \frac{\partial \mu_i^{(j)}}{\partial \boldsymbol{r}_i} \right] & \text{if } i \in [n,m] \\ 0 & \text{if } i \notin [n,m] \end{cases} \tag{33}$$

Similar to the previous case, substituting the average element temperature $T_i$ at each element $i$ into the constraint 12, we obtain the partial derivative of $g$ with respect to $\boldsymbol{T}_f$ for the material-specific

temperature constraints as

$$\frac{\partial g}{\partial \boldsymbol{T}_f} = \left[\sum_{i=n}^{m}\left(\sum_{j=2}^{4}(\mu_i^{(j)})^{\eta}\frac{T_i}{T^{*(j)}}\right)^{p}\right]^{\frac{1}{p}-1} \cdot \begin{bmatrix} \sum_{i=n}^{m}\sum_{j=2}^{4}\left(\frac{(\mu_i^{(j)})^{\eta}}{T^{*(j)}}\right)^{p} T_i^{p-1}\varphi_i^{(1)} \\ \vdots \\ \sum_{i=n}^{m}\sum_{j=2}^{4}\left(\frac{(\mu_i^{(j)})^{\eta}}{T^{*(j)}}\right)^{p} T_i^{p-1}\varphi_i^{(s)} \end{bmatrix}_{s\times 1} \tag{34}$$

where

$$\varphi_i^{(l)} = \frac{\partial T_i}{\partial t_f^{(l)}} = \begin{cases} 1/4 & \text{if } \frac{\partial T_i}{\partial t_f^{(l)}} \neq 0 \\ 0 & \text{if } \frac{\partial T_i}{\partial t_f^{(l)}} = 0 \end{cases}, l = 1, \cdots, s. \tag{35}$$

*2.6. Density Filtering*

When implementing element-based topology optimization methods, results may be susceptible to numerical instabilities such as checkerboarding and mesh-dependency [38]. To avoid such phenomena, we employ a filtering method that is analogous to the density filter method [39] used in the SIMP formulation. Here, we apply the filter to the parameters, $r_1$ and $r_2$. By introducing the independent design parameter $x_{1_i}$ and $x_{2_i} \in [0, 1]$ for each element $i$, we can compute the effective design parameters of $r_{1_i}$ and $r_{2_i}$ for element $i$ as a weighted sum of the independent parameters for all elements within a prescribed neighborhood of element $i$, as follows.

$$r_{j_i} = \sum_{k\in\Omega_i} \omega_{ik} x_{j_i} / \sum_{k\in\Omega_i} \omega_{ik}, \text{ for } j = 1, 2; \;\; i = 1, 2, ...n \tag{36}$$

where $n$ is the number of elements in the finite element mesh, $\Omega_i$ represents the neighborhood over which the density filter is active, and $\omega_{ik}$ is a weight value that depends on the distance $d_{ik}$ between element $i$ and element $k$ as shown below, with $d^*$ denoting the radius of the filter neighborhood.

$$\omega_{ik} = \begin{cases} d^* - d_{ik} & \text{if } d_{ik} < d^* \\ 0 & \text{if } d_{ik} \leq d^* \end{cases} \tag{37}$$

## 3. Result and Discussion

*3.1. Case 1: Optimal Thermal Response*

Generally, topology optimization problems in which we seek to promote dissipation of thermal energy (i.e. by minimizing average global temperature) result in a branch-like topological layouts. To verify that our proposed methodology produces reasonable results that are consistent with previous work on this topic, we first generate results for a purely thermal problem in which we minimize the global average temperature in the structure, subject to a constraint on the total material volume. The corresponding numerical optimization problem statement can be written as follows.

$$\begin{aligned} \min f_{obj} &= \frac{\sum_{i=1}^{n}(1-\mu_i^{(1)})T_i}{\sum_{i=1}^{n}(1-\mu_i^{(1)})} \\ s.t \quad & V \leq 0.3 \end{aligned} \tag{38}$$

Here $T_i$ is the average temperature within element $i$ as defined in equation 10, and $\mu_i^{(1)}$ is the activation function for the void phase. The fraction $V$ is the volume ratio, which is defined as

the fraction of the working domain that is occupied by non-void elements. Hence, the objective function here represents the average temperature of the structure excluding the void regions.

The geometry and boundary conditions for the thermal design problem are shown in Fig. 1(a). We first begin with a single-material case, using Beryllium Copper for the solid phase. The optimization results are shown in Fig. 2. For illustrative purposes, we set the temperature in the void area to be zero when plotting the temperature distribution in the optimized structures.


(a) Material distribution (b) Temperature Distribution

Figure 2: Optimized topology for the single material domain with thermal response, $f_{obj} = 84.12°\text{C}$

From the above figure we can see that the resulting material layout is indeed tree-like. We obtain a similar result when solving the same design problem using a multimaterial approach. Figures 3 and 4 show the optimized material layout and temperature distribution for the multimaterial problem.

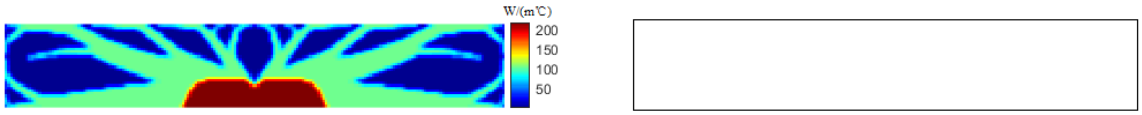


(a) Material distribution by thermal conductivity (b) SAC305

(c) BC (d) Al-SiC

Figure 3: Optimized topology for the multimaterial domain with thermal response, $f_{obj} = 78.24°\text{C}$

Comparing the optimization result of the multimaterial case with the single material case, we can see that the multimaterial design has lower average temperature. This result demonstrates that by expanding the design space to allow for multiple materials, we are able to obtain superior designs with improved thermal response. Meanwhile, we also observe that in the multimaterial case for the pure thermal optimization problem, in order to lower the energy transfer, the optimizer tends to choose material with low thermal conductivity throughout most of the structure; while in the pure elastic optimization problem, the optimizer will have a preference for the stiffest possible material, which generally translates to a high thermal conductivity. Hence, we can expect that there will be a trade off in which the optimizer must balance the conflicting elastic and thermal

design considerations. This tradeoff will be discussed further in the later sections.


Figure 4: Temperature distribution for the multimaterial domain with thermal repsonse

### *3.2. Optimal Design for Combined Elastic and Thermal Response*

#### *3.2.1. Case 2: Minimization of Structural Compliance and Average Temperature*

In the case of a combined thermoelastic objective, we again begin with the single material case, using Beryllium Copper for the solid material phase. The combined objective is stated in equation 9 and the numiercal optimization problem for both the single and multimaterial problem is given by

$$\begin{aligned} \min f_{obj} &= \frac{\boldsymbol{F}^T\boldsymbol{u}}{\boldsymbol{F}^T\boldsymbol{u}_0} + \left(\frac{\sum_{i=1}^{n}(1-\mu_i^{(1)})T_i}{\sum_{i=1}^{n}(1-\mu_i^{(1)})}\right) / \left(\frac{\sum_{i=1}^{n}(1-\mu_{0_i}^{(1)})T_{0_i}}{\sum_{i=1}^{n}(1-\mu_{0_i}^{(1)})}\right) \\ s.t \quad & V \leq 0.3 \end{aligned} \tag{39}$$

Similar to the purely thermal design problem, the only optimization constraint is the constraint on the volume fraction. For the elastic analysis, we assume plane stress conditions. The optimized topology and temperature distribution are shown in Fig.5.


(a) Material distribution (b) Temperature Distribution

Figure 5: Optimized topology for the single material domain with combined thermoelastic objective, $f_{obj} = 0.1290$, compliance= 14.21N·m, $T_{\text{ave}} = 76.13°\text{C}$

From this result we can see that in addition to the standard truss structure, the design contains branches jutting out from the truss. These branches provide heat dissipation, which is demanded by the thermal term in the combined objective function. For the multimaterial case, the result is very similar, as shown in Fig.6 and Fig.7

From the multimaterial result, we can see that both the elastic compliance and the average temperature field are lower than that of the single material design. This result is consistent with our hypothesis that the multimaterial framework better enables the optimizer to pursue conflicting design objectives by optimally distributing multiple design materials with disparate material characteristics.

#### *3.2.2. Case 3: Compliance Minimization with a Maximum Temperature Constraint*

In Case 3, we minimize the structural compliance subject to a constraint on the maximum local temperature along the top surface of the structure. The statement of this optimizing problem is

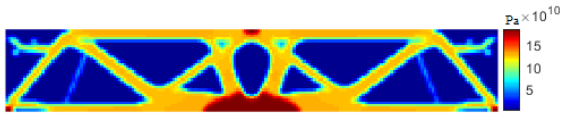


(a) Material distribution by Young's modulus

(b) SAC305

(c) BC

(d) Al-SiC

Figure 6: Optimized topology for the multimaterial domain with combined thermoelastic objective, $f_{obj} = 0.1156$, compliance= 11.03N·m, $T_{\text{ave}} = 74.21°\text{C}$


Figure 7: Temperature distribution for the multimaterial domain with a combined objective function

shown below in equation 40.

$$\begin{aligned} &\min f_{obj} = \boldsymbol{F}^T \boldsymbol{u} \\ &s.t \quad g = \left[ \sum_{i=n}^{m} \left( (1 - \mu_i^{(1)})^{\eta} \frac{T_i}{T^*} \right)^p \right]^{1/p} \leq 1 \\ &\quad V \leq 0.3 \end{aligned} \tag{40}$$

The maximum allowable temperature along the top surface is set to $T^*30°\text{C}$. The geometry and boundary conditions for both the elastic and thermal problems is given in Fig. 1. Figure 8 shows the optimized material distribution for the multimaterial design, while Fig. 9 displays the temperature field within the optimized structure.

The result shows that the algorithm has successfully converged to a feasible design, with the maximum temperature on the top surface reaching 27.6857°C. In this case, the constraint is active, however the maximum temperature is slightly below the prescribed threshold ($T^* = 30°\text{C}$) due the the conservative nature of the $p$-norm approximation. An interesting observation is that, to satisfy the constraint, the optimizer will directly place more void elements at the area with highest temperature, to impede propagation of heat energy to the rest of the structure. This means the bottom area with a fixed temperature will be more slender than in the results obtained for cases 1 and 2.

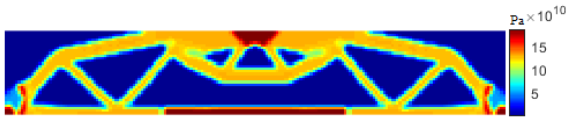


(a) Material distribution by Young's modulus

(b) SAC305

(c) BC

(d) Al-SiC

Figure 8: Optimized topology for the multimaterial domain with a maximum temperature constraint, $f_{obj} = 18.23\text{N}\cdot\text{m}$


Figure 9: Temperature distribution for multimaterial domain with a maximum temperature constraint

*3.2.3. Case 4: Compliance Minimization with a Material-Specific Temperature Constraint*

In the final example, we solve the same thermoelstic design problem described above, however we implement a material-specific constraint on the local temperature, which is defined in equation 12. As in the previous case, we minimize compliance subject to a 30% volume constraint. The maximum allowable temperature throughout the domain is set to 35% of the melting point of each material, since this is the temperature at which creep effects can be observed in metals [40]. Since 35% of the melting point of SAC305 is too low to set as a restriction, we choose an alternative material, Magnesium alloy, AZ91, whose Young's modulus and thermal conductivity are very close to SAC305, but has a higher melting point. The material properties used in this case are shown below in Table 2.

| Material | Void | AZ91 | BC | Al-SiC |
|---|---|---|---|---|
| $E$(GPa) | $10^{-9}$ | 42 | 131 | 188 |
| $\kappa$(W/(m·°C)) | 0.5 | 70 | 105 | 200 |
| Melting Point(°C) | - | 550 | 955 | 613 |
| Creep constraint(°C) | - | 15.0 | 156.0 | 37.1 |

Table 2: Material properties

In this problem, the fixed (i.e. applied) temperature was set to 37.5% of the melting point of the stiffest material (Al-SiC), which yields $\overline{T} = 63.5°\text{C}$ at the bottom center of the domain boundary. The results of this case are shown in Fig.10 and Fig.11.

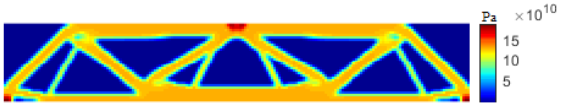


(a) Material distribution by Young's modulus

(b) AZ91

(c) BC

(d) Al-SiC

Figure 10: Optimized topology for the multimaterial domain with material-specific temperature constraints, $f_{obj} = 17.34\text{N}\cdot\text{m}$


Figure 11: Temperature distribution for multimaterial domain with material-specific temperature constraints

In this result, the highest temperature and the lowest temperature of each material are shown below in Table 3. As shown in the table, the optimized design is feasible, with none of the material-specific temperature limits being breached. In this example, the constraint is active only for the middle material, Al-SiC, while the material with the highest melting point remains well below its own prescribed temperature limit, but does reach temperatures above the maximum for the other two materials. This example demonstrates that we can effectively enforce multiple material-specific temperature limits using a single global constraint function.

| Material | AZ91 | BC | Al-SiC |
|---|---|---|---|
| Max Temperature(°C) | - | 63.50 | 37.09 |
| Max allowable Temperature(°C) | 15.0 | 156.0 | 37.1 |

Table 3: Maximum and minimum temperatures of each design material

### *3.3. An Alternative Domain Geometry*

To further validate the proposed algorithm, we test it on a second design problem with an alternative domain geometry. Specifically, we seek to verify the multimaterial case with a single temperature constraint on the maximum temperature at the top surface of the domain, as defined in equation 40. The new design domain is a 6m×6m square domain with all the remaining parameters unchanged from the previous example. The load $p$ still has a magnitude of 100kN, and the fixed temperature is set to $\overline{T} = 100°\text{C}$ at the bottom center. The heat flux remains $q = 50\text{w/m}^2$. The available design materials are identical to those used in case 3, SAC305, Beryllium Copper, Al-SiC

plus the void phase. The optimized results for the square domain, under a temperature constraint of $T^* = 30°\text{C}$ are shown in Fig.13 and Fig.14.

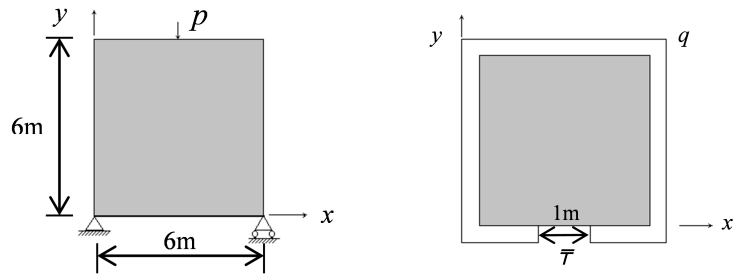


(a) Elastic boundary conditions (b) Thermal boundary conditions

Figure 12: Geometry and boundary conditions for the thermoelastic problem with square design domain

The results are similar to those obtained in Case 3 above, with the constraint being active, and a maximum temperature of 26.5342°C on the top surface. Here again, the optimizer has placed the material with the highest stiffness at the areas of high stress, while a slender bar component is placed along the bottom surface to slow down energy transfer.

## 4. Conclusions

We have presented a novel method for multimaterial topology design for optimal elastic and thermal responses. The uncoupled elastic and steady-state thermal responses were simulated using linear finite element analysis, and the material distribution was parameterized using the SFP formulation. Each design material was characterized according to its elastic modulus and its thermal conductivity. Results confirmed that for design problems that combine elastic and thermal considerations, the multimaterial formulation produced superior structures, as the optimizer was able to optimally allocate multiple materials with disparate thermal and elastic properties to pursue conflicting design goals.

In addition to optimizing a hybrid objective function that combined the elastic compliance and average temperature, we also optimized for elastic compliance subject to a constraint on the maximum local temperature along the top surface of the design domain. Furthermore, we performed a similar optimization in which we enforced material-specific maximum temperature limits. For this task we implemented a novel formulation in which the average temperature within each element was expressed as a fraction of the creep limit for the specific material within that element, and the resulting normalized temperature values were aggregated using a the $p$-norm function to obtain a global constraint function. Results demonstrated that this formulation could be used to effectively generate feasible multimaterial structures in which each material domain remains within its prescribed temperature range.

## 5. Acknowledgements

This research was supported by the National Science Foundation through grant number CMMI-1663566.

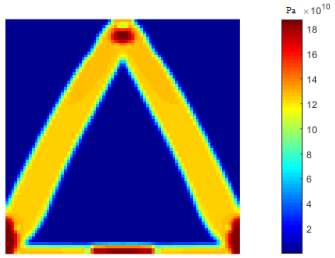


(a) Material distribution by Young's modulus

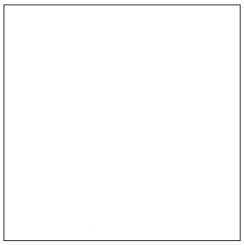

(b) SAC305

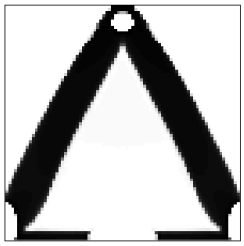

(c) BC

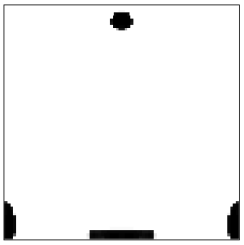

(d) Al-SiC

Figure 13: Optimized topology for multimaterial square domain with a maximum temperature constraint

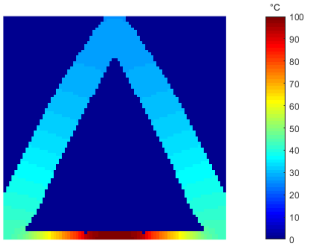


Figure 14: Temperature distribution for the multimaterial square domain with a maximum temperature constraint

## References


[1] Bendsøe, Martin Philip, and Noboru Kikuchi. Generating optimal topologies in structural design using a homogenization method. *Computer methods in applied mechanics and engineering* 71.2 (1988): 197-224.

[2] A. Gaynor, N. Meisel, C. Williams, J. Guest, Multiple-material topology optimization of compliant mechanisms created via Polyjet three-dimensional printing, Journal of Manufacturing Science and Engineering 136 (2014) 1–10.

[3] Eschenauer, Hans A., and Niels Olhoff. Topology optimization of continuum structures: a review. *Applied Mechanics Reviews* 54.4 (2001): 331-390.

[4] Uwe Schramm, Ming Zhou. Recent Developments in the Commercial Implementation of Topology Optimization. *IUTAM Symposium on Topological Design Optimization of Structures, Machines and Materials: Status and Perspectives* 239248; 2006 Springer.

[5] Bendsøe, Martin Philip, and Ole Sigmund. Topology optimization: theory, methods, and applications. 2nd edtion *Springer Science & Business Media,* 2004.

[6] Duysinx, Pierre, and Martin P. Bendsøe. Topology optimization of continuum structures with local stress constraints. *International journal for numerical methods in engineering* 43.8 (1998): 1453-1478.

[7] Pereira, J. T., E. A. Fancello, and C. S. Barcellos.. Topology optimization of continuum structures with material failure constraints. *Structural and Multidisciplinary Optimization* 26.1 (2004): 50-66.

[8] Pars, J., F. Navarrina, I. Colominas, and M. Casteleiro. Topology optimization of continuum structures with local and global stress constraints. *Structural and Multidisciplinary Optimization* 9, no. 4 (2009): 419-437.

[9] Bendsøe, Martin P., and Ole Sigmund. Material interpolation schemes in topology optimization. *Archive of applied mechanics* 69.9 (1999): 635-654.

[10] Sigmund, Ole, and Salvatore Torquato. Design of materials with extreme thermal expansion using a three-phase topology optimization method. *Journal of the Mechanics and Physics of Solids* 45.6 (1997): 1037-1067.

[11] Li, Ying, Kazuhiro Saitou, and Noboru Kikuchi. Topology optimization of thermally actuated compliant mechanisms considering time-transient effect. *Finite elements in analysis and design.* 40.11 (2004): 1317-1331.

[12] Maute, Kurt, Stefan Schwarz, and Ekkehard Ramm. Adaptive topology optimization of elastoplastic structures. *Structural and Multidisciplinary Optimization* 15.2 (1998): 81-91.

[13] Schwarz, Stefan, Kurt Maute, and Ekkehard Ramm. Topology and shape optimization for elastoplastic structural response. *Computer Methods in Applied Mechanics and Engineering* 190.15 (2001): 2135-2155.

[14] Jung, Daeyoon, and Hae Chang Gea. Topology optimization of nonlinear structures. *Finite Elements in Analysis and Design* 40.11 (2004): 1417-1427.

[15] Li, Q., Steven, G. P., Xie, Y. M., Querin, O. M. Evolutionary topology optimization for temperature reduction of heat conducting fields. *International Journal of Heat and Mass Transfer* 47, no. 23 (2004): 5071-5083.

[16] Zhuang, ChunGang, ZhenHua Xiong, and Han Ding. A level set method for topology optimization of heat conduction problem under multiple load cases. *Computer methods in applied mechanics and engineering* 196.4 (2007): 1074-1084.

[17] Lohan, Danny J., Ercan M. Dede, and James T. Allison. Topology optimization for heat conduction using generative design algorithms. *Structural and Multidisciplinary Optimization* (2015): 1-15.

[18] Gersborg-Hansen A., Bendsoe MP., Sigmund O. Topology optimization of heat conduction problems using the finite volume method. *Structure Multidisciplinary Optimization* 31 (2006):251259.

[19] Dede, Ercan M. Multiphysics topology optimization of heat transfer and fluid flow systems. *proceedings of the COMSOL Users Conference.* 2009.

[20] Chen, Yuhang, Shiwei Zhou, and Qing Li. Multiobjective topology optimization for finite periodic structures. *Computers & Structures* 88.11 (2010): 806-811.

[21] Burger, Francois H., Jaco Dirker, and Josua P. Meyer. Three-dimensional conductive heat transfer topology optimisation in a cubic domain for the volume-to-surface problem. *International Journal of Heat and Mass Transfer* 67 (2013): 214-224.

[22] Bruns, Tyler E. Topology optimization of convection-dominated, steady-state heat transfer problems. *International Journal of Heat and Mass Transfer* 50.15 (2007): 2859-2873.

[23] Iga, A., S. Nishiwaki, K. Izui, and M. Yoshimura. Topology optimization for thermal conductors considering design-dependent effects, including heat conduction and convection. *International Journal of Heat and Mass Transfer* 52, no. 11 (2009): 2721-2732.

[24] Dede, Ercan M., Shailesh N. Joshi, and Feng Zhou. Topology optimization, additive layer manufacturing, and experimental testing of an air-cooled heat sink. *Journal of Mechanical Design* 137.11 (2015): 111403.

[25] de Kruijf, Niek, Shiwei Zhou, Qing Li, and Yiu-Wing Mai. Topological design of structures and composite materials with multiobjectives. *International Journal of Solids and Structures* 44.22 (2007): 7092-7109.

[26] M. P. Bendsøe, O. Sigmund Material interpolation schemes in topology optimization *Archive of Applied Mechanics* 69 (1988) 635-654.

[27] R. Tavakoli. Multimaterial topology optimization by volume constrained AllenCahn system and regularized projected steepest descent method *Computer methods in applied mechanics and engineering* 276 (2014): 534-565.

[28] J. Blasques. Multi-material topology optimization of laminated composite beams with eigenfrequency constraints *Composite Structures* 111 (2014): 4555.

[29] S. Jeong, D.-H. Choi, G. Yoon. Separable stress interpolation scheme for stress-based topology optimization with multiple homogenous materials *Finite Elements in Analysis and Design* 82 (2014): 16-31.

[30] T. Gao, W. Zhang. A mass constraint formulation for structural topology optimization with multiphase materials. *Journal for Numerical Methods in Engineering* 88 (2011): 774-796.

[31] P. Liu, Y. Luo, Z. Kang. Multi-material topology optimization considering interface behavior via xfem and level set method *Computer Methods in Applied Mechanics and Engineering* 308 (2016): 113-133.

[32] M. Cui, H. Chen, J. Zhou. A level-set based multi-material topology optimization method using a reaction diffusion equation *Computer-Aided Design* 73 (2016): 41-52.

[33] Y. Wang, Z. Luo, Z. Kang, N. Zhang. A multi-material level set-based topology and shape optimization method *Computer Methods in Applied Mechanics and Engineering* 283 (2015): 1570-1586.

[34] KA. James. Multiphase Topology Design with Optimal Material Selection Using an Inverse P-Norm Function *International Journal for Numerical Methods in Engineering* (2017).

[35] http://www.engineeringtoolbox.com/.

[36] Bruyneel, Michal, Pierre Duysinx, Claude Fleury, and Tong Gao. Extensions of the shape functions with penalization parameterization for composite-ply optimization. *AIAA journal* 49, no. 10 (2011): 2325-2329.

[37] Gao, Tong, Weihong Zhang, and Pierre Duysinx. A bivalue coding parameterization scheme for the discrete optimal orientation design of the composite laminate. *International Journal for Numerical Methods in Engineering* 91.1 (2012): 98-114.

[38] O. Sigmund, S. Torquato. Design of smart composite materials using topology optimization. *Smart Material Structure* 8 (1998): 365-379.

[39] C. Le, J. Norato, T. Bruns, C. Ha, D. Tortorelli. Stress-based topology optimization for continua. *Structure Multidiscplinary Optimization* 41 (2010): 605-620.

[40] William D. Callister Jr., David G. Rethwisch. Materials Science and Engineering: An Introduction. *Wiley* (2013).

[41] K. Svanberg, The method of moving asymptotes - a new method for structural optimization, Int. J. Numer. Meth. Optim. 24 (1987) 359–373.